JOURNAL OF GEOPHYSICAL RESEARCH, VOL. 104, NO. D19, PAGES 23,899–23,909, OCTOBER 20, 1999

Seasonal and interannual variability of the budgets of N_2O and CCl_3F

Sun Wong[1]
Department of Physics, Columbia University, New York

Michael J. Prather
Department of Earth System Science, University of California at Irvine

David H. Rind
Institute for Space Studies, NASA Goddard Space Flight Center, New York

Abstract. The 6-year wind archives from the Goddard Institute for Space Studies/Global Climate-Middle Atmosphere Model (GISS/GCMAM) were input to the GISS/Harvard/Irvine Chemical Transport Model (G/H/I CTM) to study the seasonal and interannual variability of the budgets and distributions of nitrous oxide (N_2O) and trichlorofluoromethane (CCl_3F), with the corresponding chemical loss frequencies recycled and boundary conditions kept unchanged from year to year. The effects of ozone feedback and quasi-biennial oscillation (QBO) were not included. However, the role of circulation variation in driving the lifetime variability is investigated. It was found that the global loss rates of these tracers are related to the extratropical planetary wave activity, which drives the tropical upward mass flux. For N_2O a semiannual signal in the loss rate variation is associated with the interhemispheric asymmetry in the upper stratospheric wave activity. For CCl_3F the semiannual signal is weaker, associated with the comparatively uniform wave episodes in the lower stratosphere. The loss rates lag behind the wave activity by about 1–2 months. The interannual variation of the general circulation model generated winds drives the interannual variation of the annually averaged lifetime. The year-to-year variations of the annually averaged lifetimes can be about 3% for N_2O and 4% for CCl_3F.

1. Introduction

The relationship between the stratospheric wave activity and the meridional distribution of long-lived tracers was discussed by *Holton* [1986]. The isopleths of a long-lived tracer are balanced by the transport due to diabatic circulation, horizontal eddy transport, and chemical loss in the stratosphere. The diabatic circulation steepens the isopleths, but both the horizontal eddy transport and the chemical loss tend to flatten the isopleths. Since both the diabatic circulation and the horizontal eddy transport are controlled by wave activity [*Holton*, 1986; *Holton et al*., 1995], the effects of wave activity on the long-lived tracer distributions are complicated. Greater wave activity can steepen the isopleths across subpolar latitudes by strengthening the diabatic circulation, but flatten the isopleths by enhancing the horizontal eddy transport. The effect of these opposing mechanisms was well illustrated by the different rates of descent of methane (CH_4) and N_2O in the polar vortex [*Strahan et al*., 1996].

In the tropics the upward mass flux across the tropopause is controlled by the extratropical wave activity [*Haynes et al*., 1991; *Holton et al*., 1995]. The annual mean of the mass flux across the tropical 100 mbar surface is estimated to be 85×10^8 kg/s with significant seasonal variation (114×10^8 kg/s in December-January-February (DJF) and 56×10^8 kg/s in June-July-August (JJA)) [*Rosenlof and Holton*, 1993]. This seasonal variation of the tropical upward mass flux induces an observable annual cycle of lower stratospheric temperatures in the tropics [*Yulaeva et al*., 1994; *Rosenlof*, 1995, and references therein]. Interannual variation of the tropical upward mass flux was also derived from United Kingdom Meteorological Office (UKMO) assimilated temperatures and National Meteorology Center (NMC) temperatures [*Rosenlof*, 1995].

Both N_2O and CCl_3F are long-lived tracers with tropospheric sources, and not effectively removed in the troposphere. They are transported into the stratosphere through the tropical tropopause and dissociated in the stratosphere by chemical processes, providing constituents that trigger the catalytic destructions of stratospheric ozone. The N_2O lifetime derived from observations is about 120 years [*Prather et al*., 1994; *Minschwaner et al*., 1998] and 124 ± 49 years [*Volk et al*., 1997], and that derived from previous two-dimensional (2-D) models is in the range of 120–139 years [*Ko and Jackman*, 1994]. The CCl_3F lifetime derived from observations is 50 years [*Prather et al*., 1994], 34–47 years [*Ko and Jackman*, 1994], 52^{+23}_{-12} years [*Cunnold et al*., 1997], and 41 ± 12 years [*Volk et al*., 1997], and that derived from the 2-D models is 40–60 years [*Ko and Jackman*, 1994].

In this paper, the seasonal and interannual variability in the N_2O and CCl_3F lifetimes is examined with a 3-D model, which is required for investigation of the impacts of planetary wave on the tracers' budgets since parameterization for the eddy

[1]Now at Atmospheric Sciences Research Center, Albany, New York.

Paper number 1999JD900776.
0148-0227/99/1999JD900776$09.00

Table 1. Seasonal and Interannual Variability in the N_2O and CCl_3F Lifetimes

Year	January	April	July	October	Annual Mean
		N_2O			
1	109.3	118.4	130.2	129.8	122.2
2	109.8	120.5	125.5	124.8	120.2
3	109.6	118.6	129.7	129.8	121.1
4	108.5	125.1	129.7	128.4	123.2
5	107.2	115.7	129.6	125.4	119.9
6	110.7	119.0	126.3	123.6	120.5
Average	109.2	119.6	128.5	127.0	121.2
Maximum changes, %	3.2	7.9	3.7	3.9	2.7
		CCl_3F			
1	30.3	30.1	34.1	31.2	31.5
2	29.8	29.7	33.2	30.0	30.6
3	29.9	30.5	34.0	31.4	31.3
4	30.2	31.3	34.3	31.1	31.8
5	29.7	30.3	34.2	30.7	31.5
6	31.1	31.1	33.6	29.0	31.1
Average	30.2	30.5	33.9	30.6	31.3
Maximum changes, %	4.6	5.2	3.2	7.8	3.8

Lifetimes are in years. Note: In last column are the annual mean lifetimes, and in the last row of each section are the largest peak-to-peak interannual differences in the corresponding columns (in percentage about the corresponding column mean values).

transport are not necessary in 3-D models. The interannual variation in ozone transport and quasi-biennial oscillation (QBO) are not included. This paper is the first step to understand the role of the variation in wave activity in driving the lifetime variations, without any feedback from ozone response and modulation by QBO. In section 2 the models used are described. Section 3 discusses the simulation results. Discussion and conclusions are included in section 4.

2. Models

The tracer experiments used the 21-layer Chemical Transport Model (CTM) [*Prather*, 1993], which advects chemical constituents with winds produced from the 23-layer Goddard Institute for Space Studies Global Climate-Middle Atmospheric Model (GISS/GCMAM) [*Rind et al*., 1988a, b]. The GISS/GCMAM has been analyzed for a range of climate change experiments [*Rind et al*., 1990, 1992; *Rind and Balachandran*, 1995; *Rind and Lonergan*, 1995; *Shindell et al*., 1997]. The CTM adopts the $7.83° \times 10°$ grid of the parent general circulation model (GCM) for its horizontal resolution and uses vertical layers extending from the surface to 0.004 mbar (about 85 km). The tropospheric layers, from 1 to 9, use sigma coordinates, while the stratospheric layers, from 10 to 21, use fixed pressure levels beginning above 100 mbar. The top three layers of the 23-layer GCM are combined into the top layer of the CTM.

Boundary conditions for trace gas mixing ratios are applied in the lowest three layers (up to 1 km), which can be either fixed or varying in time. The chemistry of N_2O and CCl_3F is parameterized by their zonally and monthly averaged loss frequencies. These parameters are calculated from a photochemical box model using observed climatic values for temperature, ozone, and other trace gases [*Avallone and Prather*, 1997; *Prather and Jaffe*, 1990]. Parameterized convection and the associated horizontal diffusion occur in the troposphere, but not in the stratosphere. The advecting scheme conserves first- and second-order moments of the tracer distribution [*Prather*, 1986]. The CTM has been used to study tropospheric distribution of CFCs, dilution of the ozone hole, the space shuttle impacts, seasonal evolutions of N_2O, O_3, and CO_2, and tracer-tracer correlations [*Avallone and Prather*, 1997; *Hall and Prather*, 1993, 1995; *Prather et al*., 1987, 1990, 1994].

The GISS/GCMAM was used to produce 6-year wind archives and the associated diagnostics, especially Eliassen-Palm (E-P) flux convergence which is a representative for planetary wave activity. The model provides generally realistic interannual variability in the mean circulations and planetary wave activity [*Rind et al*., 1988b]. The primary deficiencies of the model are somewhat reduced long-wave energy in the troposphere and lower stratosphere, too cold temperatures near the model top, and too warm temperatures in the southern hemisphere polar lower stratosphere.

Initial tracer distributions were calculated by recycling the first year of the GCM winds until a near steady state repeating annual cycle was reached. The subsequent 5 years of winds are then put into the CTM sequentially. These runs are referred to as SEQUENTIAL runs. In order to compare our results with the steady state results, we ran another set of experiments in which each year's wind was recycled for about 10 years until a near steady state was reached for that year's wind archive. These are referred to as STEADYSTATE runs (i.e., we have six individual near steady state distributions for the corresponding 6-year wind archives). Since we initialized the tracers with the first year steady state distributions, all the first year results in the SEQUENTIAL runs match those in the STEADYSTATE runs. For all the experiments the chemical loss frequencies and the tropospheric convection processes (not very important in these experiments) were recycled from year to year. The fixed chemical loss frequencies are equivalent to fixing the overhead column ozone amount; therefore feedbacks from ozone response are not allowed in this study. The boundary condition of N_2O was fixed at 300 ppbv, and that of CCl_3F was fixed at 250 parts per trillion by volume (pptv) for the lowest three levels of the CTM.

3. Results

3.1. Lifetimes

The lifetime of a chemical tracer is defined as the total mass (in kg) divided by the globally integrated loss rate (in kg/yr). Since the boundary conditions were fixed, the total mass of both tracers did not vary significantly over the years. Hence the lifetimes are inversely proportional to the loss rates in our simulation results. The difference in global loss rates between the SEQUENTIAL and STEADYSTATE runs is small (about 3–4% from the mean values, see Figures 2 and 3) for our 6 years of meteorology. The differences in tracer distributions throughout the stratosphere are also small. Hereafter, our discussion will concentrate on the SEQUENTIAL runs.

Table 1 shows the seasonal and interannual variability of the lifetimes of both tracers in the SEQUENTIAL runs. The largest interannual difference in annual-mean lifetimes is about 3% for N_2O and about 4% for CCl_3F about their mean lifetimes. For both tracers the seasonal variability is larger than the interannual variability. The interannual variability in the

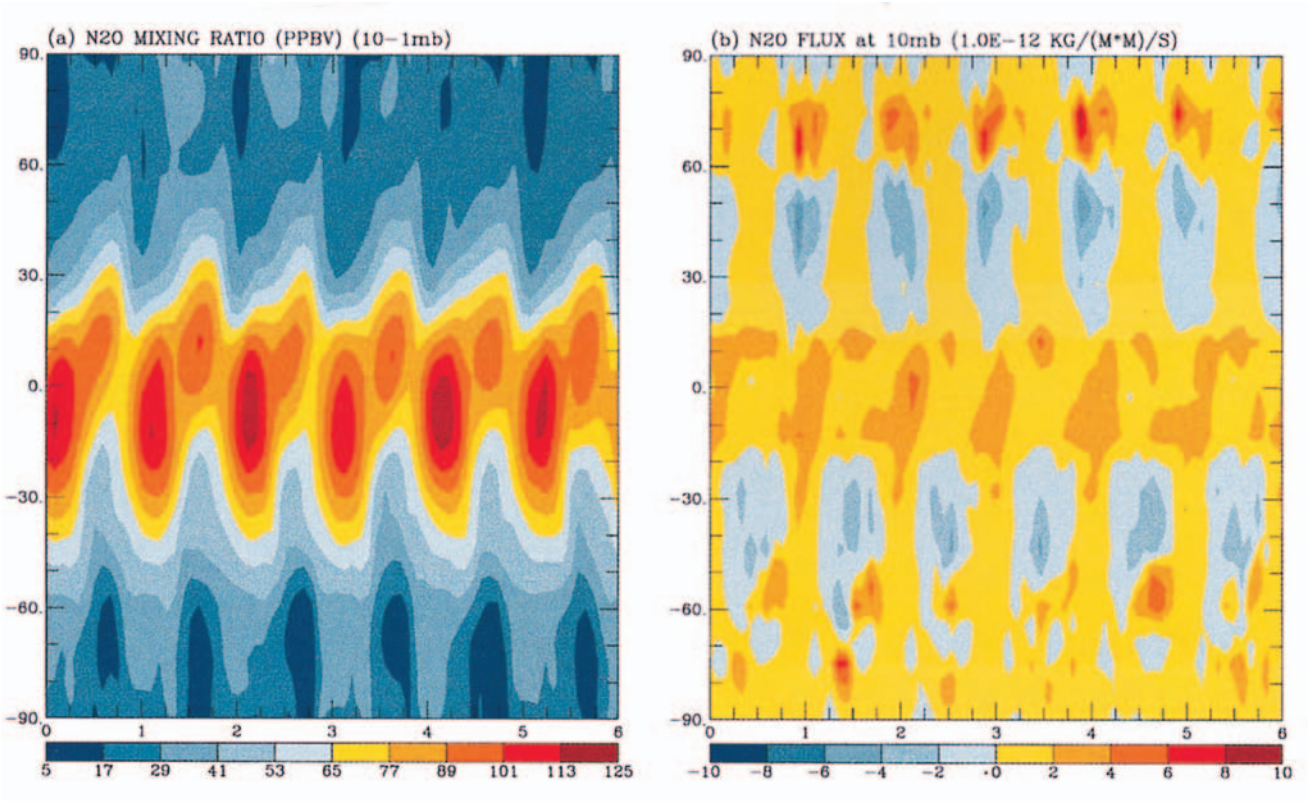

Plate 1. Evolution of the N_2O distribution and flux. (a) The zonal mean N_2O mixing ratio (in ppbv) averaged from 10 to 1 mbar; (b) the zonal mean N_2O flux (in 10^{-12} kg m^{-2} s^{-1}) across 10 mbar. The x axis is for simulation year, and the y axis is for latitude.

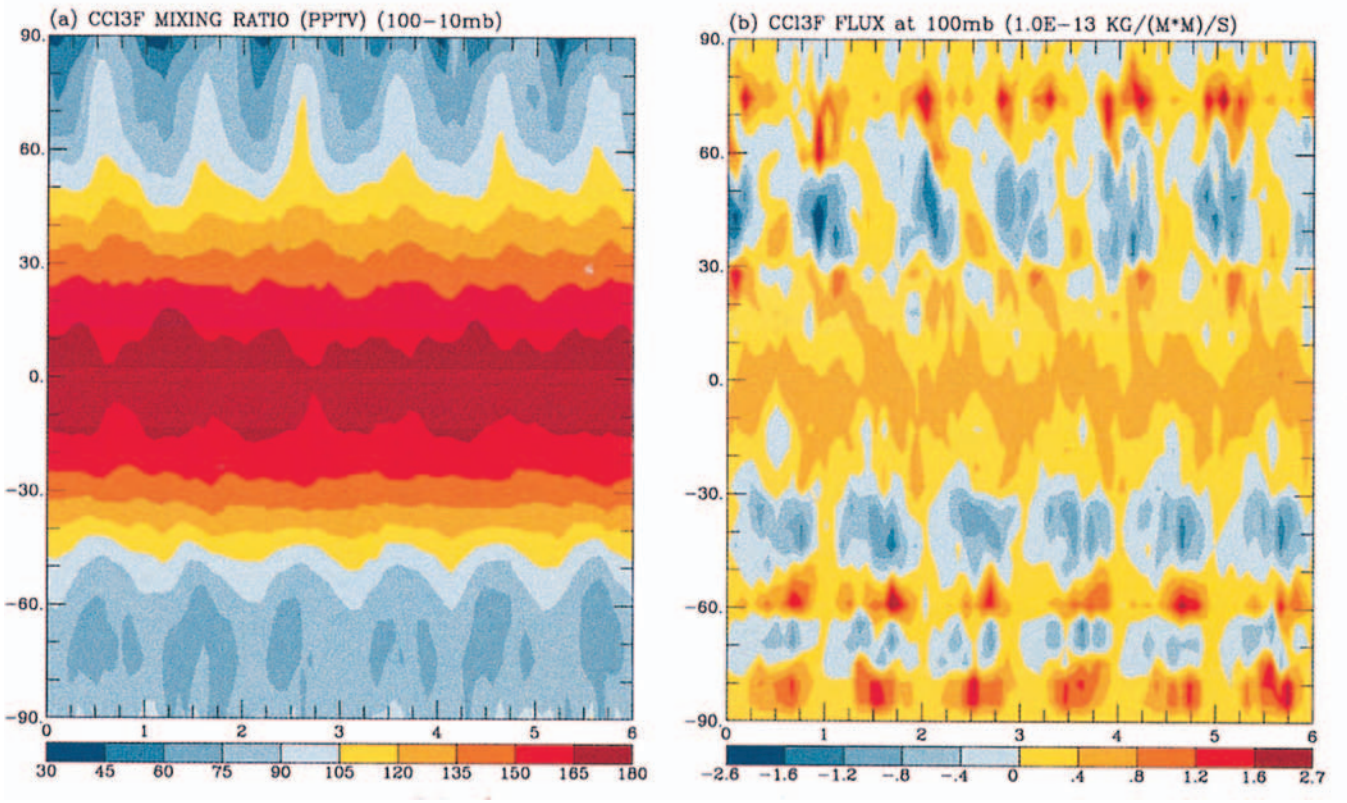

Plate 2. Evolution of the CCl_3F distribution and flux. (a) The zonal mean CCl_3F mixing ratio (in pptv) averaged from 100 to 10 mbar; (b) the zonal mean CCl_3F flux (in 10^{-13} kg m^{-2} s^{-1}) across 100 mbar. The x axis is for simulation year, and the y axis is for latitude.

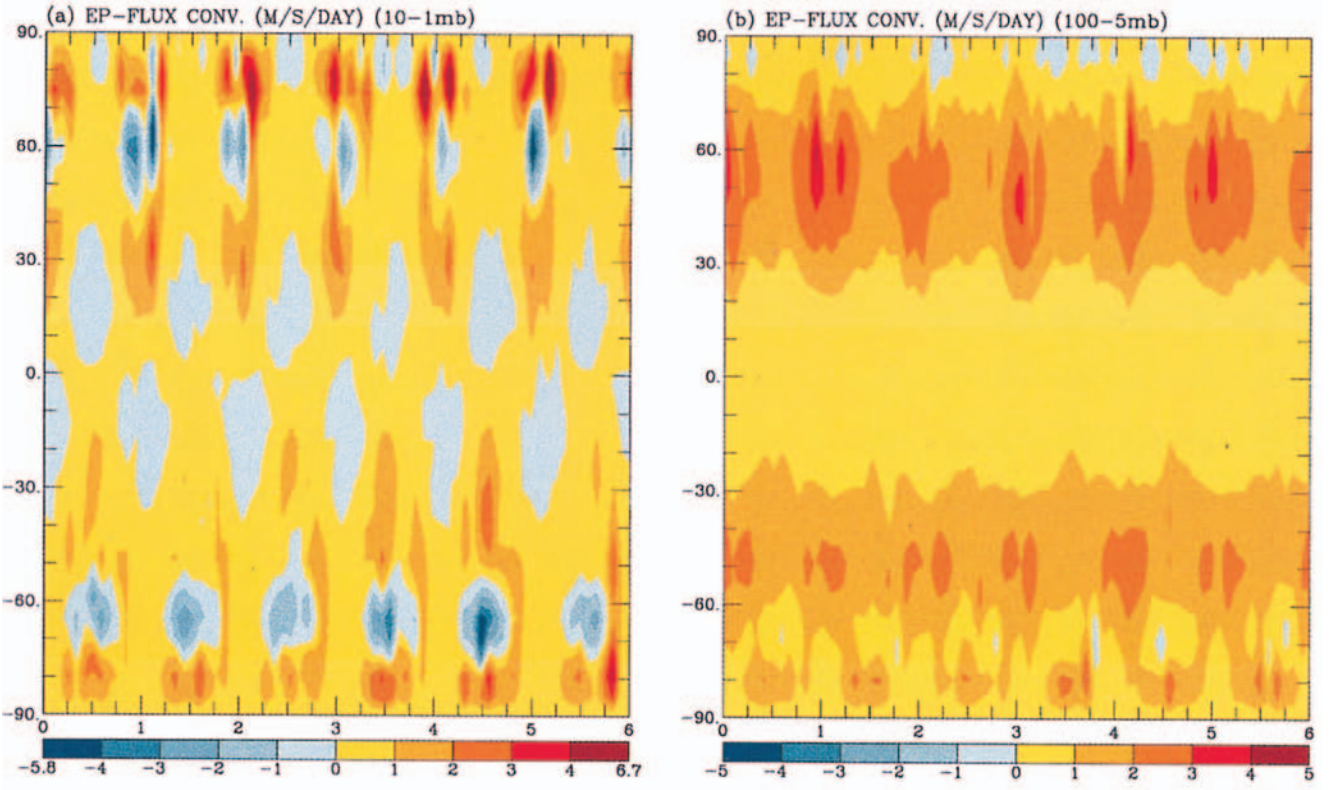

Plate 3. Evolution of the model stratospheric planetary wave activity, represented by the E-P flux convergence (in m s^{-1} d^{-1}). (a) Averaged from 10 to 1 mbar; (b) averaged from 100 to 5 mbar. The x axis is for simulation year, and the y axis is for latitude.

spring seasons (i.e., April (APR) or October (OCT)) is larger than that in the solstices (i.e., January (JAN) or July (JUL)). However, the interannual variability is reduced when the annual mean lifetime is taken. The model N_2O lifetime covers the range of 107–130 years, with the climatological mean of 121 years, consistent with those of *Mahlman et al*. [1986], *Minschwaner et al*. [1998], and *Prather et al*. [1994]. The model CCl_3F lifetime covers the range of 30–34 years, with the climatological mean of 31.3 years, lower than those of *Cunnold et al*. [1997], *Ko and Jackman et al*. [1994], and *Volk et al*. [1997]. This discrepancy in the CCl_3F lifetime may be due to the coarse vertical resolution (about 5 km in the stratosphere) applied by the CTM, which produces vertical mixing that is too rapid up to about 25 km [*Avallone and Prather*, 1997].

3.2. Distributions

Since the N_2O loss is dominant in the upper stratosphere, the evolution of the zonal mean N_2O mixing ratio, averaged from 10 to 1 mbar, is shown in Plate 1a. In the tropics there are primary peaks of mixing ratio, centered at about 10°S, during January to March, and secondary peaks of mixing ratio, centered at about 10°N, during June to September. These peaks of mixing ratio also correspond to the peaks of the loss rate shown in Figure 2. The location and time of the peaks agree with previous studies of the Cryogenic Limb Array Etalon Spectrometer (CLAES) data [*Randel et al*., 1994; *Lou et al*., 1997], in which primary peaks of N_2O mixing ratio were centered around 10°S during January to March in 1992 and 1993, while a secondary peak was centered around 10°N during August to October in 1992. However, it is hard to tell if the primary and secondary peaks had difference in magnitudes from these previous studies, although the model result of *Lou et al*. [1997] showed that the primary peaks had larger magnitude than the secondary peak at 10 mbar. The annual cycle of the N_2O mixing ratio shown in Plate 1a is also in general agreement with that of the CH_4 mixing ratio shown by *Randel et al*. [1998, Figure 9]. The primary peak of CH_4 mixing ratio at 2.2 mbar was found during February to March, centered at about 10°S, and the secondary peak with about the same magnitude of the primary peak was found during August to September, centered at about 10°N. At 10 mbar peak of CH_4 mixing ratio reached maximum at the equator from November to June [*Randel et al*., 1998, Figure 9]; therefore one can expect the secondary peak is smaller in magnitude if the CH_4 mixing ratio is averaged from 10 to 1 mbar.

Plate 1b shows the evolution of the zonal mean N_2O flux across 10 mbar. In the tropics, primary peaks of upward flux occur in December–January, whereas secondary peaks of upward flux occur in June, with magnitudes smaller than those of the primary peaks. The evolution of the mixing ratio is consistent with that of the flux, with a time lag of 1–2 months, that is, from midwinter, when the flux is maximum, to late winter and early spring, when the mixing ratio is maximum. In high latitudes, peaks of upward flux can be seen around 70°N or 60°S, where polar descent (downward motion) should be expected. The zonal mean tracer flux includes the mean and eddy fluxes and resembles the pattern of zonal mean circulation, instead of the Transformed Eulerian Mean (TEM or the residual) circulation, because the eddy flux is about 2–3 order of magnitude smaller. Therefore the pattern of the zonal mean flux shown in Plate 1b (as well as in Plate 2b for CCl_3F) is consistent with the multicell structure of the zonal mean circulation, and the upward flux seen around 70°N or 60°S is an extension of the

upward branch of the polar and the Ferrel cells from the troposphere. However, the polar upward flux occurring during polar nights less affects the lifetime and its variation because the loss is dominant in the tropics to the subtropics.

Similar results can be obtained for CCl_3F if we consider a region in the lower stratosphere because of the predominant CCl_3F loss in this region. Plate 2a shows the zonal mean CCl_3F mixing ratio, averaged from 100 to 10 mbar, and Plate 2b shows the CCl_3F upward flux across 100 mbar. The seasonal evolution of subtropical to midlatitude CCl_3F mixing ratios (see the contour lines of 105–150 pptv in Plate 2a) agrees with that of the CH_4 mixing ratio at 68 mbar in the work of *Randel et al*. [1998], who found that the contour lines shift northward during July and southward during December to January as in our case of CCl_3F mixing ratios. However, the CCl_3F mixing ratio in the tropics shows less variability than those of N_2O and CH_4 at the same levels. This may be due to the fact that CCl_3F has larger photochemical loss in the tropics and behaves less as an passive tracer in this region. The seasonal variability of CCl_3F mixing ratio recovers in higher latitudes where the photochemical loss is smaller.

3.3. Planetary Wave Activity and Upward Tracer Fluxes

The extratropical "suction pump" is believed responsible for driving the tropical upward mass flux which brings in tracers from the troposphere [*Haynes et al*., 1991; *Holton et al*., 1995]. The theory suggests that the tropical upward mass flux is related to the extratropical wave activity, including both planetary and subgrid scale waves. Here we will consider only the impacts of planetary wave activity. Plate 3 shows the model evolution of planetary wave activity, represented by the E-P flux convergence averaged from 10 to 1 mbar in Plate 3a, and from 100 to 5 mbar in Plate 3b. In order to justify that the GISS/GCMAM has proper variability in planetary wave activity, the E-P flux divergence derived from NMC data from 1981–1995 is shown in Figure 1 [*Randel*, 1992] (note that Figure 1 plots the E-P flux divergence so the shaded negative regions should be compared with the red positive regions in Plate 3). In the upper stratosphere (10–1 mbar, Plate 3a and top panel of Figure 1) the model E-P flux convergence in middle latitudes reaches 2–3 m s^{-1} d^{-1} in northern hemisphere and 1–2 m s^{-1} d^{-1} (2–3 m s^{-1} d^{-1} in the fourth year) in southern hemisphere. This is consistent with the NMC E-P flux data, about 2.5 m s^{-1} d^{-1} in most of the years (5 m s^{-1} d^{-1} in some of the years) in northern hemisphere, and about 0–2.5 m s^{-1} d^{-1} (over 2.5 m s^{-1} d^{-1} in some of the years) in southern hemisphere. In the northern polar region, maxima over 5 m s^{-1} d^{-1} are seen in some of the years in both the model and NMC data. In the lower stratosphere (100–5 mbar, Plate 3b and bottom panel of Figure 1) the model E-P flux convergence generally agrees with the NMC E-P flux convergence (2–3 m s^{-1} d^{-1} in northern hemisphere and 1–2 m s^{-1} d^{-1} in southern hemisphere). In both upper and lower stratosphere the model can provide reasonable variability in planetary wave activity.

In the upper stratosphere (Plate 3a), strong wave episodes occur during autumn to early spring from 8° to 40° in latitude and drive larger tropical upward tracer flux. The interhemispheric asymmetry in the winter wave activity is associated with the seasonal asymmetry in the tropical upward flux, as well as the seasonal asymmetry in the N_2O loss. In the lower stratosphere (Plate 3b), wave episodes cover a range in time and latitude (from 8° to 72°) that is wider than those in the upper stratosphere. The interhemispheric asymmetry in wave activity is less evident in the lower stratosphere. The distinction between primary and secondary peaks of the tropical CCl_3F flux and mixing ratio is also less evident.

The E-P flux convergence shown in Plate 3 is consistent with the tracer flux patterns shown in Plates 1b and 2b. In the upper stratosphere, peaks of downward tracer flux across 10 mbar (Plate 1b) occur when the tropical upward tracer flux is at its maxima. This is because the E-P flux convergence from 20° to 40° (Plate 3a) provides poleward transport while the E-P flux divergence from 50° to 70° provides equatorward transport. The resultant horizontal tracer flux convergence produces downward tracer flux from 40° to 50° due to mass continuity. The downward tracer flux continues to lower altitude as shown in Plate 2b. In the 100 mbar level (Plate 2b) the upward tracer flux appearing in the southern polar region is stronger than that in the northern polar region and may shift the springtime total ozone maxima toward lower latitudes in the southern hemisphere. This is consistent with the previous observational and model evolution of the total ozone, in which maxima of total ozone are seen during southern spring in the southern subpolar region (about 400 Dobson units (DU) around 50°–60°S in September to October), whereas the maxima of total ozone during northern spring occur within the northern polar region (about 440 DU around 80°–90°N in March to April) [*Bowman and Krueger*, 1985; *Ushimaru and Tanaka*, 1994].

3.4. Time Series

Time series of several averaged variables, representing different physical processes, are shown in Figures 2 and 3 for N_2O and CCl_3F, respectively. Different tracers have different regions of dominant loss, and so only data in appropriate regions are used to produce the corresponding time series. Figure 2a is the averaged E-P flux convergence from 8° to 40° in latitude and from 10 to 1 mbar in altitude, a region where the planetary wave activity is responsible for the tropical upward flux across 10 mbar. The red and blue lines represent the northern and southern wave activity, respectively. The tropical upward flux is driven by the combination of wave activity in both hemispheres; therefore the sum is also plotted as the black line. The spikes occurring during November to March are mainly from the northern wave episodes, whereas those occurring during May to October are mainly from the southern wave episodes. Figure 2b is the N_2O flux averaged from 24°S to 24°N, a latitude range in which the N_2O flux is upward in the tropics, at 10 mbar (Plate 1b). The time series of the flux is correlated with that of the wave activity.

Figures 2c and 2d show the variations of the global N_2O loss rate and mixing ratio, respectively. The mixing ratio is averaged from 30°S to 30°N in latitude and from 10 to 1 mbar in altitude, a region in which the averaged N_2O mixing ratio reflects the tropical concentration variation (see Plate 1a). The black lines are from the STEADYSTATE runs, and the red dotted lines are from the SEQUENTIAL runs. Primary peaks of mixing ratio occur during January to March, whereas secondary peaks occur during August to October, with magnitudes smaller than those of the primary peaks. This semiannual signal in the loss rate and the mixing ratio resembles the semiannual signal in the tropical upward flux across 10 mbar (Figure 2b), which is driven by the asymmetric wave forcing from both hemispheres (Figure 2a). This result is consistent with *Rosenlof* [1995, Figure 15] in which a semiannual signal in the tropical upward mass flux above 10 mbar was detected.

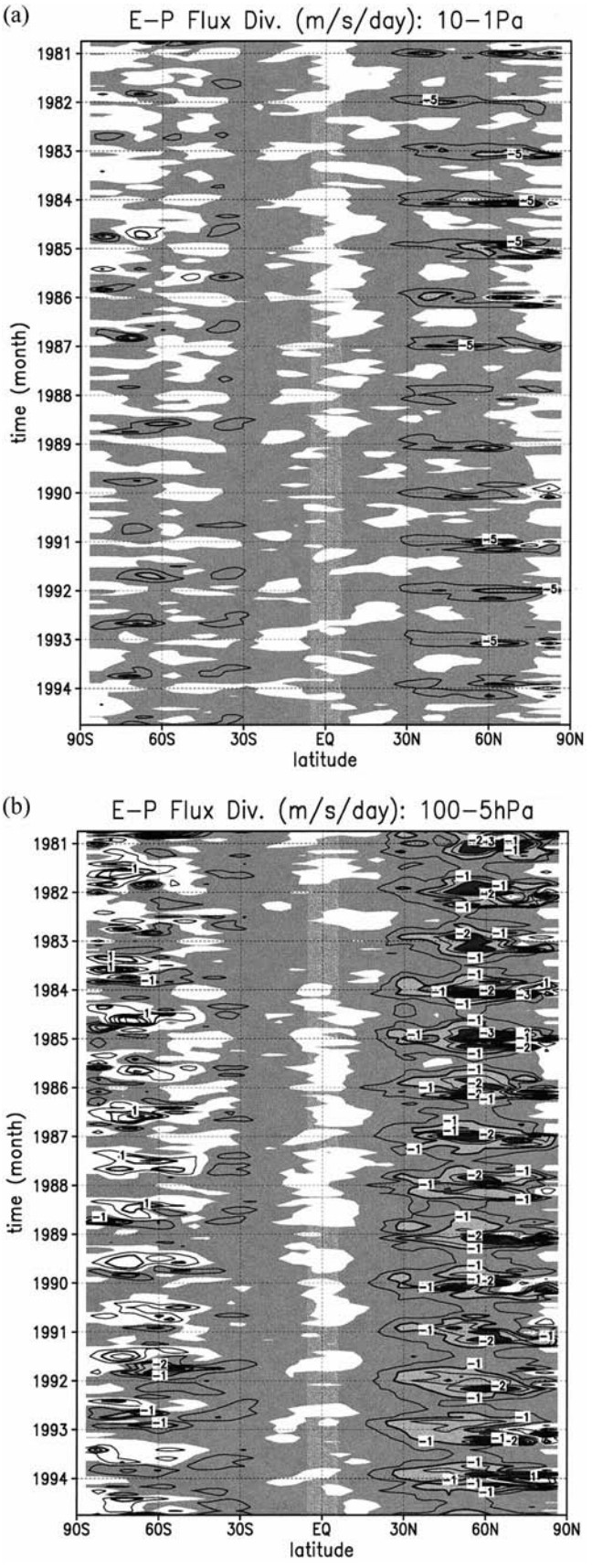

Figure 1. Evolution of the NMC stratospheric planetary wave activity, represented by the E-P flux divergence (in m s^{-1} d^{-1}), averaged (top) from 10 to 1 mbar (contour interval 2.5) and (bottom) from 100 to 5 mbar (contour interval 0.5) [*Randel*, 1992].

The CCl_3F loss is dominant in the lower stratosphere, over a range of latitude wider than that found for the N_2O loss. Figure 3 is the averaged E-P flux convergence from 8° to 72° in latitude and from 100 to 5 mbar in altitude, a region in which the averaged E-P flux convergence represents about 80% of the forcing of the tropical upward mass flux [*Rosenlof*, 1995]. The symbols in Figure 3a are similar to those in Figure 2a. Peaks of wave episodes are comparatively uniform in time. However, primary peaks during January to April are still evident. Figure 3b shows the time series of the upward CCl_3F flux across the tropical tropopause, represented by the flux averaged from 30°S to 30°N at 100 mbar, a region where the tropical flux is mainly upward. The annual cycle is evident with peaks occurring during January to March. The time series of the CCl_3F loss rate and mixing ratio are shown in Figures 3c and 3d, respectively. The mixing ratio is averaged from 50°S to 50°N in latitude and from 100 to 10 mbar in altitude, a region with wider latitude range because the dominant loss of CCl_3F covers a wider range in latitude. The semiannual signal is less evident than that in the N_2O plots in Figure 2, associated with the comparatively uniform wave episodes in the lower stratosphere. This is consistent with *Rosenlof* [1995], who found that the semiannual signal has a larger amplitude above 10 mbar.

An estimate of the air mass flux across 100 mbar can be obtained if the tracer fluxes and the corresponding tracer mixing ratios right below 100 mbar are known. Table 2 shows the estimate of the tropical upward air mass flux across 100 mbar from the CTM as well as the estimates from the previous literature. Our air mass flux is smaller than the estimate by *Rosenlof and Holton* [1993] during northern winter. However, during southern winter, our air mass flux is quite consistent with *Rosenlof and Holton* [1993]. This is reasonable because GISS/GCMAM simulates weaker long wave activity and the coarse resolution cannot resolve smaller-scale processes which may govern the troposphere-stratosphere exchange [*Rind et al*., 1988a]. Also shown in Table 2 is the estimate by *Rosenlof* [1995] at 70 mbar using the UKMO assimilated temperatures. Our CTM is consistent with *Rosenlof* [1995], recalling that our data were sampled at a lower altitude (100 mbar) and thus should give slightly larger values than those at 70 mbar. For the interannual variability in the tropical upward tracer fluxes (Figures 2b and 3b), our CTM also gives reasonable variability which is similar to that shown by *Rosenlof* [1995] (their Figure 11 shows a 2-year time series of the tropical upward mass flux at 70 mbar).

3.5. Time Lag

From the correlations of the time series shown in Figures 2 and 3, one can obtain the time lag between different physical processes. Figure 4 shows these cross correlations between the adjacent time series, which are obtained from the following formula:

$$\text{corr}\ (x,y,m) = \frac{\sum_i (x_i - \bar{x})(y_i + m - \bar{y})}{\sqrt{\sum_i (x_i - \bar{x})^2 \sum_i (y_i - \bar{y})^2}} \qquad (1)$$

where m is the time lag from −12 to 12 months and overbar variables represent the mean (the average of 72 monthly data except for wave activity). For the wave activity the mean is chosen to be the offset, which is zero in Figure 2a but 1.0 in Figure 3a, because the wave activity appears as spikes instead of a Gaussian distribution around the mean. This choice of the

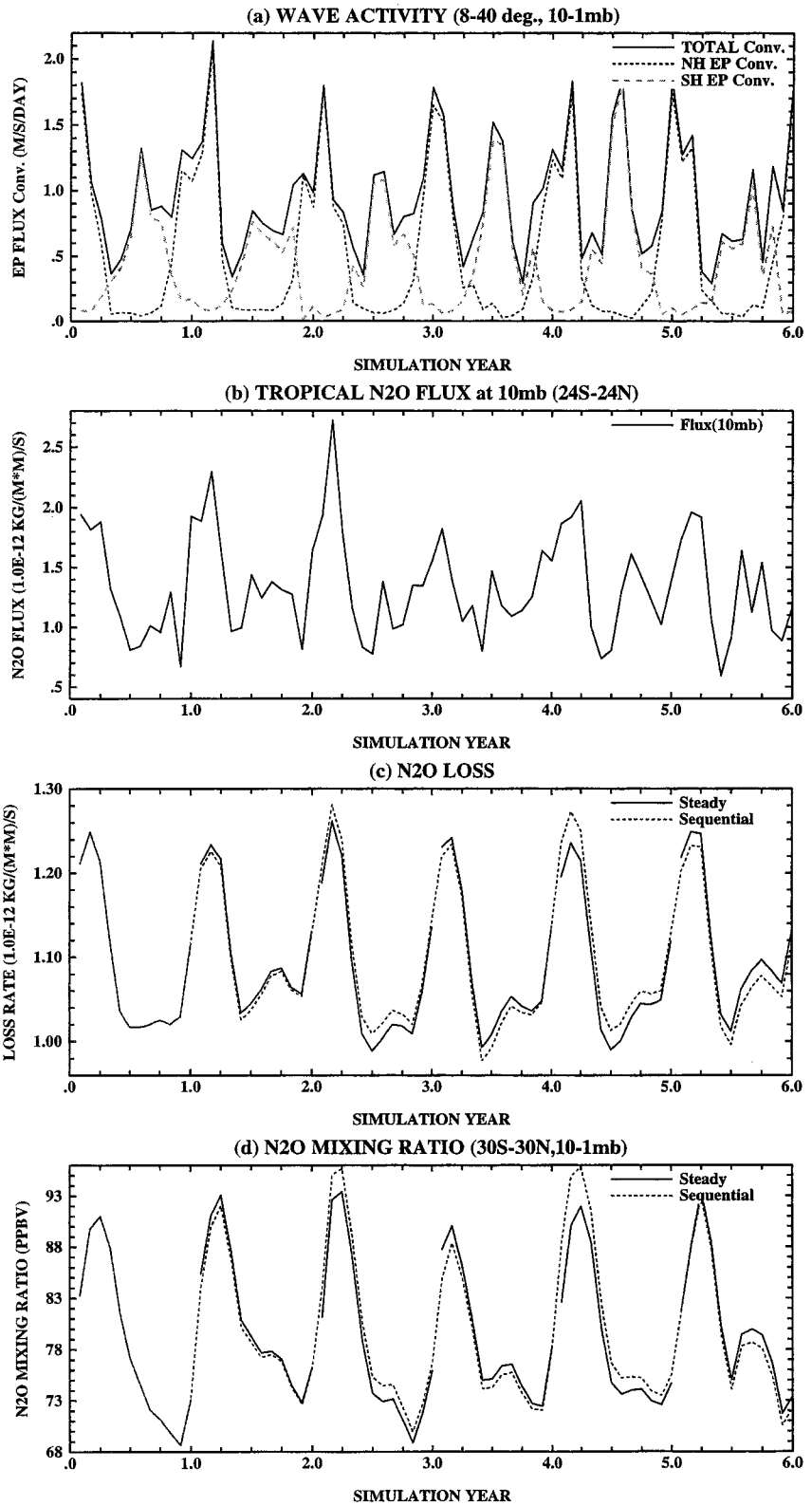

Figure 2. Time series of several averaged variables for N_2O. (a) The E-P flux convergence (in m s^{-1} d^{-1}) averaged from 8° to 40° in latitude and from 10 to 1 mbar in altitude, with the red dotted line representing the northern hemisphere, the blue dashed line denoting the southern hemisphere, and the black line indicating the sum of values from both hemispheres; (b) the tropical upward N_2O flux (in 10^{-12} kg m^{-2} s^{-1}) across 10 mbar, averaged from 24°S to 24°N in latitude; (c) the global N_2O loss rate (in 10^{-12} kg m^{-2} s^{-1}); (d) the zonal mean N_2O mixing ratio (in ppbv) averaged from 30°S to 30°N in latitude and from 10 to 1 mbar in altitude.

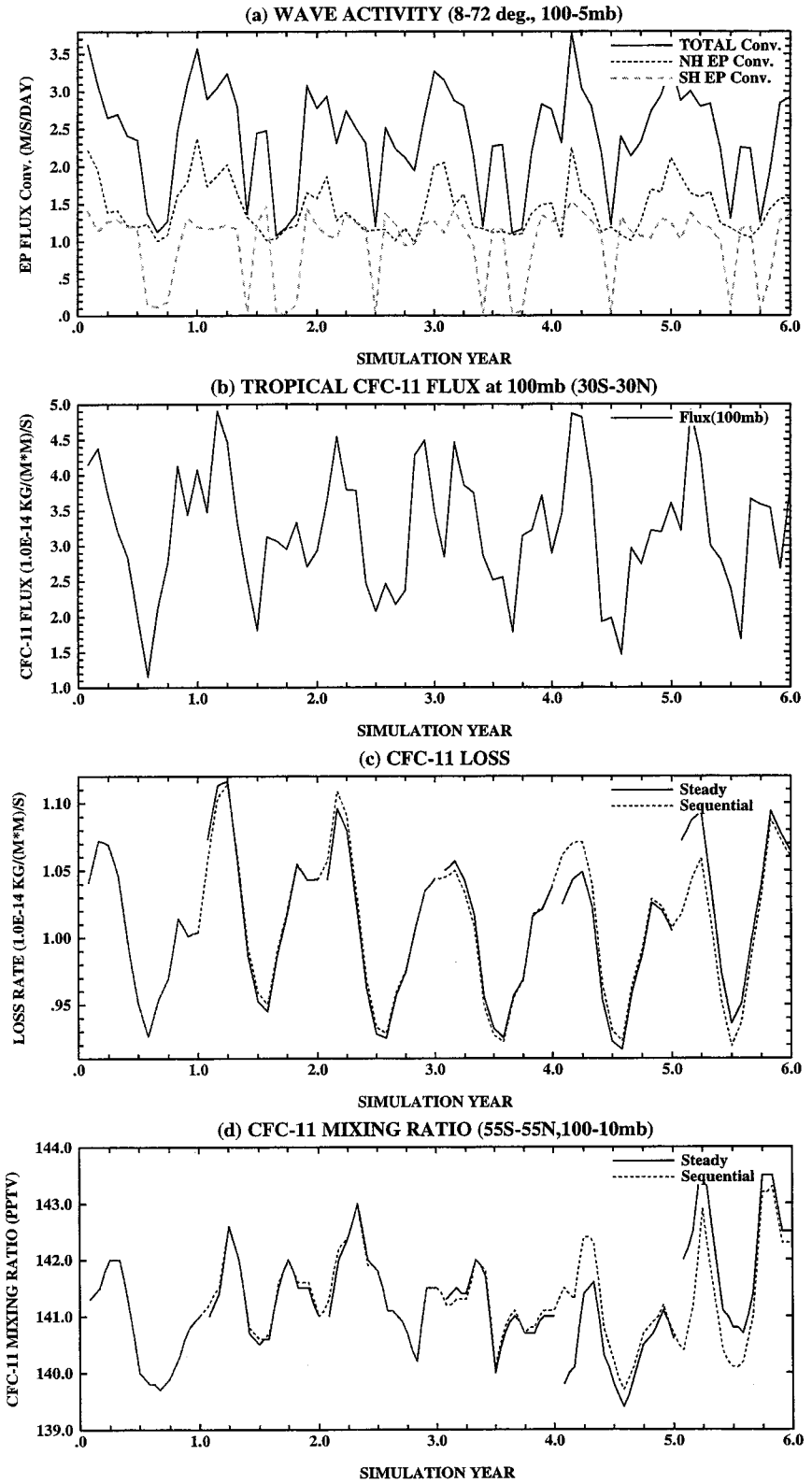

Figure 3. Time series of several averaged variables for CCl_3F. (a) The E-P flux convergence (in m s^{-1} d^{-1}) averaged from 8° to 72° in latitude and from 100 to 5 mbar in altitude, with the red dotted line representing the northern hemisphere, the blue dashed line denoting the southern hemisphere, and the black line indicating the sum of values from both hemispheres; (b) the tropical upward CCl_3F flux (in 10^{-14} kg m^{-2} s^{-1}) across 100 mbar, averaged from 30°S to 30°N; (c) the global CCl_3F loss rate (in 10^{-14} kg m^{-2} s^{-1}); (d) the zonal mean CCl_3F mixing ratio (in pptv) averaged from 55°S to 55°N in latitude and from 100 to 10 mbar in altitude.

Table 2. Comparison of the Tropical Upward Mass Flux

Data Source	DJF	JJA	Annual Mean
Rosenlof and Holton [1993]	114	56	85
Rosenlof [1995] (at 70 mbar)	66.4	43.2	54.8
Our CTM	88	50	69

Flux is in 10^8 kg s^{-1}. Note: The data of *Rosenlof* [1995] are presented at 70 mbar and for January and July only, instead of for the DJF and JJA seasons. The last column is simply the average of the DJF and JJA column data.

means for wave activity increases the correlation but does not change the time lag between different processes. Since there are clear annual cycles in the time series, peaks of correlation around ±12 months and anticorrelation around ±6 months are expected. For N_2O (Figure 4a) the tropical upward flux at 10 mbar lags the upper stratospheric wave activity by 1 month (red dotted line); the loss lags the tropical upward flux by less than 1 month (blue dashed line); and the tropical upper stratospheric mixing ratio lags the loss by about 1 month (green dash-dotted line). The direct result is that the mixing ratio lags the wave activity by about 2 months (black line). This result is consistent with *Randel et al.* [1998], who found a time lag about 1 month between the CH_4 maxima at 2.2 mbar and the tropical upward motion at the same level. Since the horizontal eddy transport counteracts the transport caused by the mean vertical wind in the tropics, the years of the maximum wave activity and the maximum tropical upward flux do not coincide for N_2O (the second year for the wave activity but the third year for the tropical upward flux).

The story is different for CCl_3F (Figure 4b) because its predominant loss is in the lower-middle stratosphere. The correlation between the tropical upward flux and the lower stratospheric wave activity is small (about 0.3) and covers a broader time range (red dotted line), which is associated with the comparatively uniform wave episodes in the lower stratosphere. The loss responds quite instantaneously to the tropical upward flux (time lag is less than 1 month, blue dashed line), and the lower stratospheric mixing ratio lags the loss by less than 1 month (green dash-dotted line). The direct correlation between the mixing ratio and the wave activity is, as expected, widespread, and it peaks at about 1 month time lag.

In our work, only planetary wave activity has been considered for the correlation calculations. GISS/GCMAM has pa-

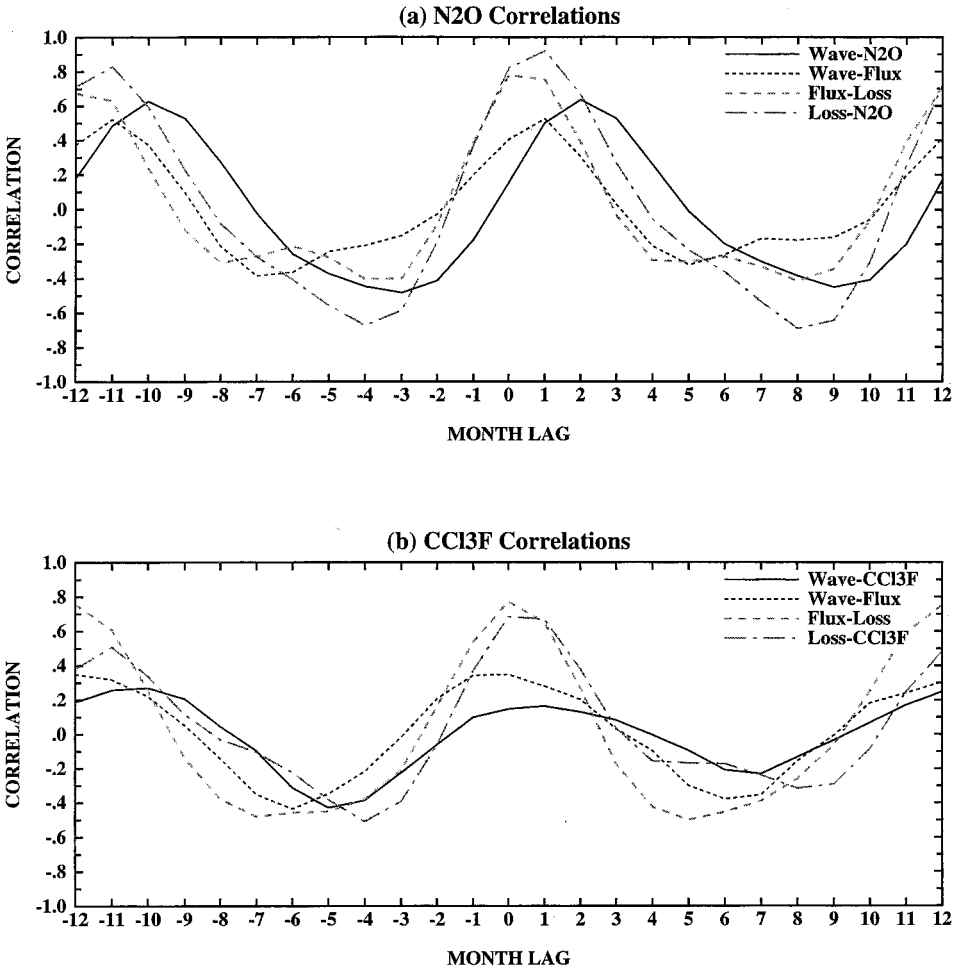

Figure 4. Time lag correlations for (a) the adjacent N_2O time series from Figure 2; (b) the adjacent CCl_3F time series from Figure 3. Red dotted lines represent correlations between the extratropical wave activity and the upward flux, blue dashed lines denote correlations between the upward flux and the global loss rate, green dash-dotted lines indicate correlations between the global loss rate and the averaged mixing ratio, and black lines designate correlations between the wave activity and the averaged mixing ratio.

rameterized gravity wave drag [*Rind et al*., 1988a] which can also drive the tropical upward mass flux. Inclusion of the gravity wave drag into the total wave activity for the correlation calculations (not shown) changes the peaks of correlation by about 10–20% but does not change the time lags discussed above.

4. Discussion and Conclusions

According to the downward control mechanism the extratropical wave activity drives the tropical upward mass flux, which brings long-lived tracers with tropospheric sources into the stratosphere. The stratospheric tracer distribution is determined by a balance between transport and photochemical loss. For N_2O the loss is dominant in the upper stratosphere, and its upper stratospheric mixing ratio lags the upper stratospheric wave activity by about 2 months. Strong wave episodes in winter induce peaks of mixing ratio in late winter to early spring. The interhemispheric asymmetry in wave activity is associated with a clear semiannual signal in the seasonal variation of the N_2O mixing ratio. For CCl_3F the loss is dominant in the lower-middle stratosphere, where wave episodes are comparatively uniform in time although northern winter peaks are still evident. The resultant seasonal variation of the CCl_3F mixing ratio has an evident annual cycle but a vague semiannual signal.

QBO, which was not simulated in our models, modulates the tropical upward mass flux in the stratosphere and contributes the majority of the interannual variance in stratospheric tracer concentrations (e.g., upper stratospheric CH_4 investigated by *Randel et al*. [1998]). Our model studies here cannot show the impacts of QBO on the interannual variation of the tracer budgets. However, the role of the model-generated variation in planetary wave activity can then be studied without the modulation of QBO. Inclusion of QBO and the relative contributions of different natural forcings (e.g., QBO, El Niño-Southern Oscillation (ENSO), and aerosol effects) in driving the interannual variation in the tropical upward mass flux need further studies by both model and observational data analyses.

In the literature, people working on CTMs usually recycle a 1-year wind archive until the models reach steady states. In this study, we see that the difference between these steady state runs and runs using subsequent wind archives with interannual variation should be small. The wind archives generated by the GISS/GCMAM produce clear seasonal and interannual variations in both the N_2O and CCl_3F budgets (e.g., their stratospheric concentrations and loss rates). This illustrates how climate change (here we have the GCM-generated wind variability) can affect long-lived tracer budgets through dynamical processes. The variation of the model tropical upward flux across 100 mbar is consistent with the air mass flux variation obtained by the radiatively determined residual circulation [*Rosenlof*, 1995]. The magnitude of the CTM air mass flux in northern winter is smaller than the result of *Rosenlof and Holton* [1993], but that in southern winter is consistent with them.

Comparing the tropical upward tracer fluxes across 100 mbar (not shown for N_2O and Figure 3b for CCl_3F) with the total loss rates (Figures 2c and 3c for N_2O and CCl_3F, respectively), we find that about one tenth of N_2O and one third of CCl_3F entering the stratosphere from the tropical tropopause is dissociated in the stratosphere (the ratio is about the ratio of the lifetimes of the two tracers if the tropospheric mixing ratios are fixed as they are in our case). The remaining amount will be transported back to the troposphere in middle to high latitudes. The variation of the ventilation through tropical tropopause may affect the concentrations of other tracers in the upper troposphere, implying variations of the upper tropospheric chemistry in the tropics. Moreover, the variation of the midlatitude downward flux across 100 mbar implies variation of the extratropical stratosphere-troposphere exchange.

The annual mean lifetimes show the largest year-to-year variability of about 3–4% about the mean values of 121 years for N_2O and 31 years for CCl_3F, smaller than the seasonal variability which is over 10% about the mean values. Upper Atmospheric Research Satellite (UARS) may provide data necessary to verify the model variations in the stratospheric mixing ratios and the tracer lifetimes [*Minschwaner et al*., 1998].

The theoretical framework by *Plumb and Ko* [1992] suggests a relation between the ratio of two tracers' lifetimes and the slope of the tracer-tracer correlation plot in the lower stratosphere,

$$\frac{\tau_1}{\tau_2} \simeq \frac{\psi_1}{\psi_2}\frac{d\psi_2}{d\psi_1} \tag{2}$$

where τ is the tracer lifetime, ψ is the tracer mixing ratio, and $d\psi_2/d\psi_1$ represents the slope of the tracer-tracer correlation plot. Scatter of data points is expected if both tracers undergo different chemistry in the stratosphere [*Avallone and Prather*, 1997; *Hall and Prather*, 1995]. Using (2), one can relate the interannual variability of tracer-tracer correlation to the interannual variability of tracer lifetimes, that is,

$$\Delta\left(\frac{d\psi_2}{d\psi_1}\right) \Big/ \left(\frac{d\psi_2}{d\psi_1}\right) \simeq \frac{\Delta\tau_1}{\tau_1} - \frac{\Delta\tau_2}{\tau_2} \tag{3}$$

where we have assumed the tropospheric mixing ratios do not have an interannual variation as they do in our simulations. From Table 1 and (3) one can imply that the interannual variability of the CCl_3F and N_2O correlation plot is about 1–4%. Therefore one cannot expect to detect it by looking at the model or observational tracer-tracer correlations because the signal is far smaller than the scatter of the plot [*Avallone and Prather*, 1997]. One can also infer that the variability of lifetimes discussed above has a very small effect on the estimates of several environmental indices which depend on the ratio of lifetimes of the tracers being concerned (e.g., Chlorine Loading Potential, etc.).

Acknowledgments. We thank William J. Randel for providing the NMC data of E-P flux divergence, Steven Pawson for preparing the plots of Figure 1, Patrick Lonergan for preparing the wind archives, Jean Lerner for providing graphic programs, and Tim Hall for invaluable discussions. We also thank the three anonymous reviewers for their invaluable comments to improve the manuscript. This work is supported by the NASA Atmospheric Chemistry and Modeling Program and the NASA Climate Program.

References

Avallone, L. M., and M. J. Prather, Tracer-tracer correlations: Three-dimensional model simulations and comparisons to observations, *J. Geophys. Res*., *102*, 19,233–19,246, 1997.

Bowman, K. P., and A. J. Krueger, A global climatology of total ozone from Nimbus 7 total ozone mapping spectrometer, *J. Geophys. Res*., *90*, 7967–7976, 1985.

Cunnold, D. M., R. F. Weiss, R. G. Prinn, D. Hartley, P. G. Simmonds,

P. J. Fraser, B. Miller, F. N. Alyea, and L. Porter, GAGE/AGAGE measurements indicating reductions in global emissions of CCl_3F and CCl_2F_2 in 1992–1994, *J. Geophys. Res.*, *102*, 1259–1269, 1997.

Hall, T. M., and R. A. Plumb, Age as a diagnostic of stratospheric transport, *J. Geophys. Res.*, *99*, 1059–1070, 1994.

Hall, T. M., and M. J. Prather, Simulations of the trend and annual cycle in stratospheric CO_2, *J. Geophys. Res.*, *98*, 10,573–10,581, 1993.

Hall, T. M., and M. J. Prather, Seasonal evolutions of N_2O, O_3, and CO_2: Three-dimensional simulations of stratospheric correlations, *J. Geophys. Res.*, *100*, 16,699–16,720, 1995.

Haynes, P. H., C. J. Marks, M. E. McIntyre, T. G. Shepherd, and K. P. Shine, On the "downward control" of extratropical diabatic circulations by eddy-induced mean zonal forces, *J. Atmos. Sci.*, *48*, 651–678, 1991.

Holton, J. R., Meridional distribution of stratospheric trace constituents, *J. Atmos. Sci.*, *43*, 1238–1242, 1986.

Holton, J. R., P. H. Haynes, M. E. McIntyre, A. R. Douglass, R. B. Rood, and L. Pfister, Stratosphere–troposphere exchange, *Rev. Geophys.*, *33*, 403–439, 1995.

Ko, M. K. W., and C. H. Jackman, Model calculations of atmospheric lifetimes, in *Report on Concentrations, Lifetimes and Trends of CFCs, Halons, and Related Species*, edited by J. A. Kaye, et al., chap. 5, pp. 5.1–5.33, Sci. Div., NASA Off. of Mission to Planet Earth, Washington, D.C., 1994.

Lou, G. P., F. N. Alyea, D. M. Cunnold, and T. P. Kindler, N_2O transport in a three-dimensional model driven by U.K. Meteorological Office winds, *J. Geophys. Res.*, *102*, 16,065–16,087, 1997.

Mahlman, J., H. Levy, and W. Moxim, Three-dimensional simulations of stratospheric N_2O: Predictions for other trace constituents, *J. Geophys. Res.*, *91*, 2687–2707, 1986.

Minschwaner, K., R. W. Carver, B. P. Briegleb, and A. E. Roche, Infrared radiative forcing and atmospheric lifetimes of trace species based on observations from UARS, *J. Geophys. Res.*, *103*, 23,243–23,253, 1998.

Plumb, R. A., and M. K. W. Ko, Interrelationships between mixing ratios of long-lived stratospheric constituents, *J. Geophys. Res.*, *97*, 10,145–10,156, 1992.

Prather, M. J., Numerical advection by conservation by second-order moments, *J. Geophys. Res.*, *91*, 6671–6681, 1986.

Prather, M. J., The atmospheric effects of stratospheric aircraft: Report of the 1992 models and measurements workshop, *NASA Ref. Publ. 1292*, *1*, 76–89, 1993.

Prather, M. J., and A. J. Jaffe, Global impact of the Antarctic ozone hole: Chemical propagation, *J. Geophys. Res.*, *95*, 3473–3492, 1990.

Prather, M. J., M. B. McElroy, S. C. Wofsy, G. Russell, and D. Rind, Chemistry of the global troposphere: Fluorocarbons as tracers of air motion, *J. Geophys. Res.*, *92*, 6579–6613, 1987.

Prather, M. J., M. M. Garcia, R. Suozzo, and D. Rind, Global impact of the Antarctic ozone hole: Dynamical dilution with a three-dimensional chemical transport model, *J. Geophys. Res.*, *95*, 3449–3471, 1990.

Prather, M. J., R. Derwent, D. Ehhalt, P. Fraser, E. Sanhueza, and X. Zhou, Other trace gases and atmospheric chemistry, in *Climate Change 1994, Radiative Forcing of Climate Change and an Evaluation of the IPCC IS92 Emission Scenarios*, edited by J. Houghton, et al., chap. 2, pp. 72–126, Cambridge Univ. Press, New York, 1994.

Randel, W. J., Global atmospheric circulation statistics, 1000–1 mb, *NCAR Tech. Note TN-366+STR*, Natl. Cent. for Atmos. Res., Boulder, Colo., 1992.

Randel, W. J., B. A. Bovile, J. C. Gille, P. L. Bailey, S. T. Massie, J. B. Kumer, J. L. Mergenthaler, and A. E. Roche, Simulation of stratospheric N_2O in the NCAR CCM2: Comparison with CLAES data and global budget analyses, *J. Atmos. Sci.*, *51*, 2834–2845, 1994.

Randel, W. J., F. Wu, J. M. Russell III, A. Roche, and J. W. Waters, Seasonal cycles and QBO variations in stratospheric CH_4 and H_2O observed in UARS HALOE data, *J. Atmos. Sci.*, *55*, 163–185, 1998.

Rind, D., and N. K. Balachandran, Modeling the effects of UV variability and the QBO on the troposphere-stratosphere system, II, The troposphere, *J. Clim.*, *8*, 2080–2095, 1995.

Rind, D., and P. Lonergan, Modeled impacts of stratospheric ozone and water vapor perturbations with implications for high-speed civil transport aircraft, *J. Geophys. Res.*, *100*, 7381–7396, 1995.

Rind, D., R. Suozzo, N. K. Balachandran, A. Lacis, and G. Russell, The GISS global climate-middle atmosphere model, I, Model structure and climatology, *J. Atmos. Sci.*, *45*, 329–367, 1988a.

Rind, D., R. Suozzo, N. K. Balachandran, A. Lacis, and G. Russell, The GISS global climate-middle atmosphere model, II, Model variability due to interactions between planetary waves, the mean circulation and gravity wave drag, *J. Atmos. Sci.*, *45*, 371–386, 1988b.

Rind, D., R. Suozzo, N. K. Balachandran, and M. J. Prather, Climate change and the middle atmosphere, I, The doubled CO_2 climate, *J. Atmos. Sci.*, *47*, 475–494, 1990.

Rind, D., N. K. Balachandran, and R. Suozzo, Climate change and the middle atmosphere, II, The impact of volcanic aerosols, *J. Clim.*, *5*, 189–208, 1992.

Rosenlof, K. H., Seasonal cycle of the residual mean meridional circulation in the stratosphere, *J. Geophys. Res.*, *100*, 5173–5191, 1995.

Rosenlof, K. H., and J. R. Holton, Estimates of the stratospheric residual circulation using the downward control principles, *J. Geophys. Res.*, *98*, 10,465–10,479, 1993.

Shindell, D. T., S. Wong, D. H. Rind, The interannual variability of the Antarctic ozone hole in a GCM, I, The influence of tropospheric wave variability, *J. Atmos. Sci.*, *54*, 2308–2317, 1997.

Strahan, S. E., J. E. Nielsen, and M. C. Cerniglia, Long-lived tracer transport in the Antarctic stratosphere, *J. Geophys. Res.*, *101*, 26,615–26,629, 1996.

Ushimaru, S., and H. Tanaka, The role of planetary waves in the formation of inter-hemispheric asymmetry in ozone distribution, *J. Meteorol. Soc. Jpn.*, *72*, 653–670, 1994.

Volk, C. M., J. W. Elkins, D. W. Fahey, G. S. Dutton, J. M. Gilligan, M. Loewenstein, J. R. Podolske, K. R. Chan, and M. R. Gunson, Evaluation of source gas lifetimes from stratospheric observations, *J. Geophys. Res.*, *102*, 25,543–25,564, 1997.

Yulaeva, E., J. R. Holton, and J. M. Wallace, On the cause of the annual cycle in tropical lower stratospheric temperatures, *J. Atmos. Sci.*, *51*, 169–174, 1994.

M. J. Prather, Department of Earth System Science, University of California at Irvine, Irvine, CA 92717. (prather@halo.ps.uci.edu)

D. H. Rind, Institute for Space Studies, NASA Goddard Space Flight Center, 2880 Broadway, New York, NY 10025. (drind@giss.nasa.gov)

S. Wong, Atmospheric Sciences Research Center, 251 Fuller Road, Albany, NY 12203. (wong@climate.cestm.albany.edu)

(Received October 20, 1998; revised June 29, 1999;
accepted July 21, 1999.)